electronic reprint

STRUCTURAL SCIENCE
CRYSTAL ENGINEERING
MATERIALS

ISSN: 2052-5206
journals.iucr.org/b

Octahedral tilting in the polar hexagonal tungsten bronzes $RbNbW_2O_9$ and $KNbW_2O_9$

Jason A. McNulty, Alexandra S. Gibbs, Philip Lightfoot and Finlay D. Morrison

Acta Cryst. (2019). B**75**, 815–821

Acta Cryst B
STRUCTURAL SCIENCE
CRYSTAL ENGINEERING
MATERIALS

ISSN 2052-5206

Octahedral tilting in the polar hexagonal tungsten bronzes $RbNbW_2O_9$ and $KNbW_2O_9$

Jason A. McNulty,[a] Alexandra S. Gibbs,[b] Philip Lightfoot[a] and Finlay D. Morrison[a]*

[a]EaStCHEM, School of Chemistry, University of St Andrews, St Andrews KY16 9ST, UK, and [b]ISIS Facility, Rutherford Appleton Laboratory, Chilton, Oxon OX11 0QX, UK. *Correspondence e-mail: finlay.morrison@st-andrews.ac.uk

Received 24 May 2019
Accepted 28 June 2019

Edited by R. Černý, University of Geneva, Switzerland

Keywords: octahedral tilting; hexagonal tungsten bronzes; X-ray diffraction; powder neutron diffraction; symmetry-mode analysis.

CCDC references: 1944138; 1944139

Supporting information: this article has supporting information at journals.iucr.org/b

The ambient-temperature structures (orthorhombic, space group $Cmc2_1$) of the polar hexagonal tungsten bronzes $RbNbW_2O_9$ and $KNbW_2O_9$ have been determined by high-resolution powder neutron diffraction. Displacement of the *A*-site cation along the polar *c* axis with concomitant octahedral tilting occurs to optimize the *A* cation bonding environment, hence reducing the coordination from 18 to 16. This effect is more evident in $KNbW_2O_9$ due to decreased *A* cation size. The octahedral tilting in both compositions results in a doubling of the *c* axis that has not previously been reported, highlighting the importance of neutron diffraction as a complementary technique for structural determination of such systems.

1. Introduction

Manipulation of composition and the effect this has on both structural and electrical behaviour of solids is the foundation of solid-state and materials chemistry. Amongst structure types composed of corner-linked octahedral units, a considerable number of studies have been carried out on both the perovskite and tetragonal tungsten bronze (TTB) structures. Each of these has a large degree of compositional and structural flexibility (Chakhmouradian & Woodward, 2014; Simon & Ravez, 2006). A related family of materials that have undergone far less extensive study is the so-called hexagonal tungsten bronzes (HTBs), which have the general formula A_xBO_3 ($x \leq 0.33$) or AB_3O_9 in the case of fully occupied *A* sites ($x = 0.33$). The HTB structure consists of corner-linked BO_6 octahedra that form hexagonal and trigonal channels down the *c* axis of the aristotype hexagonal unit cell; $a_0 \simeq 7$, $c_0 \simeq 4$ Å (Magnéli *et al.*, 1953). The *A* cation is typically a monovalent electropositive element situated in the hexagonal channel and *B* is often W^{5+}/W^{6+}. Due to the large *A*-site volume associated with the hexagonal channel compared with those associated with 'square' channels in perovskites and TTBs as well as the pentagonal channels in the latter, larger cations such as K, Rb and Cs can easily be accommodated in the HTB structure (Ivanov *et al.*, 2015).

Studies have previously been carried out investigating the effects of replacing mixed valence W with cations of a lower oxidation state to remove the conductive properties of these materials (Li *et al.*, 2017; Yanovsky *et al.*, 1983). This substitution has the effect of introducing distortions into the BO_6 octahedra *via* the second-order (pseudo) Jahn–Teller (SOJT) effect (Kunz & Brown, 1995). This type of distortion is likely to be present in both $RbNbW_2O_9$ and $KNbW_2O_9$. Although both materials have been studied previously (Lin & Bursill, 1987; Maçzka *et al.*, 2003), detailed crystallographic analysis

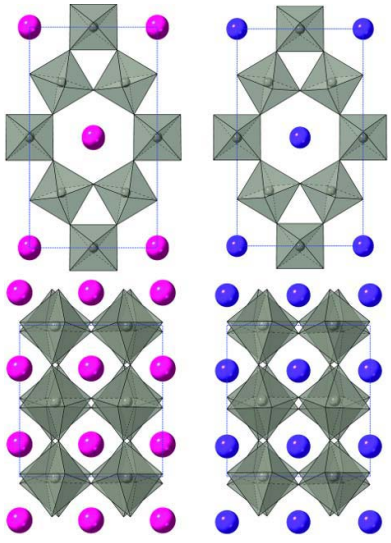

has not been carried out to the degree that the structure could be assigned unambiguously (Bursill *et al.*, 1988). Most recently, work by Chang *et al.* (2008) utilized powder X-ray diffraction (XRD) to assign both structures in the space group *Cmm*2 at ambient temperature with a large superlattice, $a \simeq 3a_0$, $b \simeq \sqrt{3}a_0$, $c \simeq c_0$. However, the published structures feature significant, perhaps unrealistic, distortions of the octahedra arising from uncertainty in the oxygen atom positions, with uncertainties as high as 0.09 Å for $B-O$ bond lengths. We now report a detailed study of both systems utilizing high-resolution powder neutron diffraction (PND), revealing some significant differences between structures determined using X-ray and neutron diffraction techniques. In particular, our study suggests a new model for these structures that exhibits a well defined octahedral tilt system driven by the size of the *A* cation in addition to SOJT distortions at the *B* sites.

2. Experimental

2.1. Synthesis

Samples were prepared *via* traditional solid-state synthesis by mixing stoichiometric amounts of Rb_2CO_3 (Sigma–Aldrich, 99%) or K_2CO_3 (Sigma–Aldrich, 99%) with Nb_2O_5 (Sigma–Aldrich, 99.9%) and WO_3 (Sigma–Aldrich, 99.9%). Reagents were dried for *ca* 1 h at an appropriate temperature (453 K for the Rb/K carbonates and 873 K for Nb_2O_5 and WO_3) prior to mixing under acetone in an agate mortar and pestle for 15 min. The resulting powders were made into pellets of 13 mm diameter and annealed at temperatures of 1173 K ($KNbW_2O_9$) and 1193 K ($RbNbW_2O_9$) for 24 h according to the procedure reported by Chang *et al.* (2008). Sacrificial powder composed of appropriate stoichiometry of unreacted reagents was used to cover the pellets to minimize alkali metal loss.

2.2. Powder diffraction

PND data were collected at ambient temperature (288 and 293 K for $RbNbW_2O_9$ and $KNbW_2O_9$, respectively) on the HRPD instrument at the ISIS facility. The samples were contained in a cylindrical vanadium can. For analysis, two detector banks covering the *d*-spacing ranges $0.7 < d < 2.6$ Å and $0.9 < d < 4.0$ Å were used.

Data were analysed by the Rietveld method using the *GSAS/EXPGUI* package (Larson & Dreele, 2004; Toby, 2001) and interpretation of the results was assisted using symmetry-mode analysis *via* the *ISODISTORT* suite (Campbell *et al.*, 2006). A consistent refinement strategy was used in each case with a 12-term shifted Chebyschev background function used to account for background coefficients. Refined variables included lattice parameters, atomic positions, isotropic atomic displacement parameters, appropriate diffractometer constants (DIFA, DIFC) and profile coefficients. Small peaks known to originate from the vanadium can were identified in the PND patterns; these were not included in the refinements.

3. Results and discussion

3.1. Structure determination from PND

Initial refinement of ambient-temperature PND data was carried out for both $RbNbW_2O_9$ and $KNbW_2O_9$ using the model determined from the earlier XRD study (Chang *et al.*, 2008). A minor additional defect pyrochlore phase ($RbNbWO_6$) is present in the Rb composition which is consistent with previous observations. For simplicity we have chosen not to incorporate this minor phase into the refinements presented here as it was present at ∼1 wt% and has a minimal contribution to the observed diffraction pattern.

Although many of the peaks observed for both compositions correspond well to those expected from the structure reported by Chang *et al.* (2008), a significant peak at $d \simeq 2.3$ Å is present that is not accounted for. This peak is present in both samples; however, the magnitude is significantly greater in $KNbW_2O_9$ and also appears to feature some degree of peak splitting that is not observed in $RbNbW_2O_9$ (Fig. 1). The absence of this peak in XRD data suggests that its origin may be attributed to the oxygen atom positions, most likely *via*

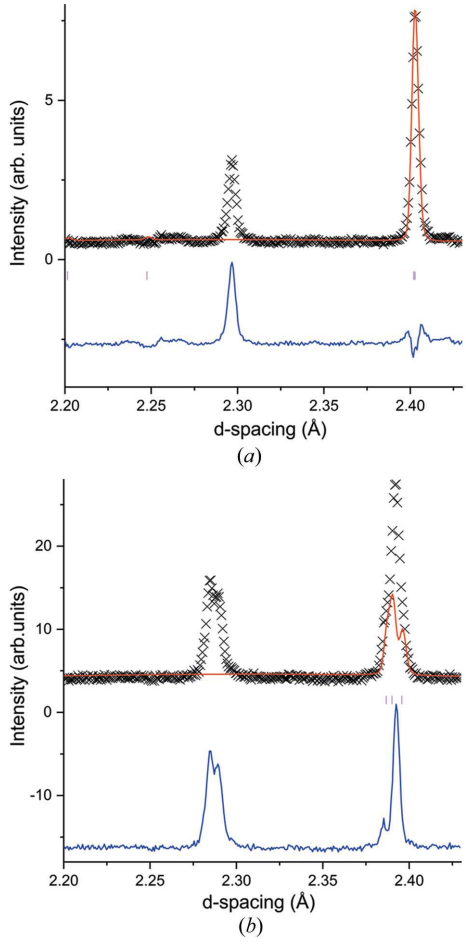

Figure 1
Portion of the Rietveld refinement profile using the Chang model (*Cmm*2) for (*a*) $RbNbW_2O_9$ and (*b*) $KNbW_2O_9$ PND data at 288 and 293 K, respectively. The peak near 2.3 Å in both (*a*) and (*b*) is caused by octahedral tilting and is not modelled in the published *Cmm*2 structures.

octahedral tilting, due to the increased sensitivity of neutron diffraction to light-atom positions.

Careful Rietveld analysis is required to ascertain the exact nature of this structural distortion. Possible octahedral tilt modes in HTBs were first predicted by Whittle *et al.* (2015) with regards to the aristotype structure, space group *P*6/*mmm*, $a_0 \simeq 7$, $c_0 \simeq 4$ Å. Their work suggested that to maintain the corner-linked network of BO_6 octahedra, tilting could only be introduced *via* the irreducible representations A_3^+ and L_2^-, resulting in models with $P6_3/mmc$ and *P*6/*mmm* symmetry and unit cells of $a_0 \times 2c_0$ and $2a_0 \times 2c_0$, respectively. The relevant points of the primitive hexagonal Brillouin zone are A: **k** = 0,0, $\frac{1}{2}$ and L: **k** = $\frac{1}{2}$, 0, $\frac{1}{2}$. A subsequent study by Campbell *et al.* (2018) acknowledged an additional tilting mode (A_6^+) leading to a *Cmcm* model in which some octahedra remain untilted. In an addendum to their initial work, Whittle *et al.* (2018) also proposed that the most likely HTB structures would have octahedral tilts of equal magnitude. The work presented by Whittle and Campbell however, does not consider the combination of tilting modes together with atomic displacements related to off-centering of *B*-site cations (*i.e.* SOJT effects).

Considering the relatively good fit of the XRD data to the published *Cmm*2 structure, initial analysis involved introduction of tilting modes into this structure. While it is not possible to introduce tilting into this model *via* the *irrep* L_2^-, incorporation of either A_3^+ or A_6^+ is possible, resulting in a $Cmc2_1$ model with a doubling of the *c* axis; *i.e.* a very large supercell, $a \simeq 3a_0$, $b \simeq \sqrt{3}a_0$, $c \simeq 2c_0$. It is worth noting that introduction of either of the A modes into this large superlattice results in simultaneous incorporation of the other, and that introduction of the A_6^+ mode leads to two possible $Cmc2_1$ models with metrics $3a_0 \times \sqrt{3}a_0 \times 2c_0$ or $\sqrt{3}a_0 \times 3a_0 \times 2c_0$ (*i.e.* where the *a* and *b* parameters have been interchanged). The group–subgroup relationships, including the associated *irreps*, of both $RbNbW_2O_9$ and $KNbW_2O_9$ are presented in Fig. S2 of the supporting information. This proposed structure remains consistent with the *Cmcm* model suggested by Whittle *et al.* (2018) but includes an additional displacive Γ_2^- mode.

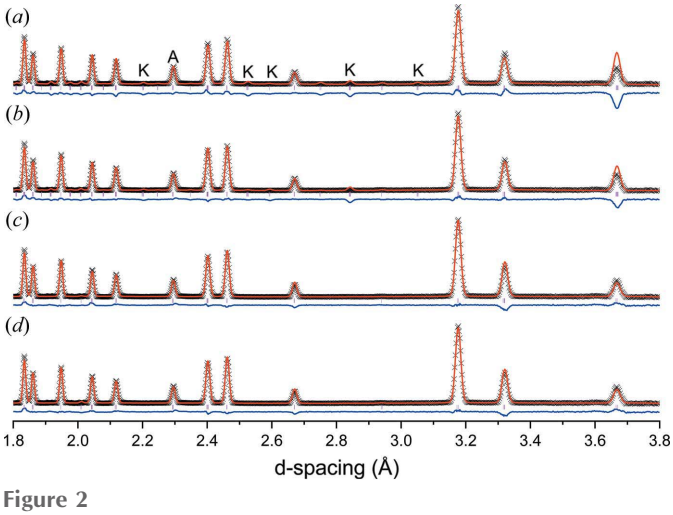

Figure 2
Portion of Rietveld refinement profiles carried out on $RbNbW_2O_9$ PND data at 288 K modelled in the space group $Cmc2_1$ featuring unit cell metrics of (*a*) $3a_0 \times \sqrt{3}a_0 \times 2c_0$; (*b*) $\sqrt{3}a_0 \times 3a_0 \times 2c_0$; (*c*) $\sqrt{3}a_0 \times a_0 \times 2c_0$; and (*d*) $a_0 \times \sqrt{3}a_0 \times 2c_0$. The peak marked 'A' represents the peak corresponding to *c* axis doubling. Note the absence of peaks (labelled 'K') corresponding to a superlattice at the K-point (**k** = $\frac{1}{3}$, $\frac{1}{3}$, 0).

Table 1
Comparison of the goodness-of-fit parameters and total number of refineable parameters (N_{tot}) of the respective Rietveld refinements for $RbNbW_2O_9$ refined in various orthorhombic space groups featuring different unit-cell dimensions.

Model	Metrics	χ^2	wR_p (%)	R_p (%)	N_{tot}
*Cmm*2	$3a_0 \times \sqrt{3}a_0 \times c_0$	39.33	11.35	7.22	72
$Cmc2_1$	$3a_0 \times \sqrt{3}a_0 \times 2c_0$	13.25	6.57	5.84	102
$Cmc2_1$	$\sqrt{3}a_0 \times 3a_0 \times 2c_0$	10.16	5.75	4.56	76
$Cmc2_1$	$\sqrt{3}a_0 \times a_0 \times 2c_0$	7.192	4.86	4.11	67
$Cmc2_1$	$a_0 \times \sqrt{3}a_0 \times 2c_0$	6.106	4.48	3.95	63

Rietveld refinement was carried for both compositions in each $Cmc2_1$ model. For brevity, only the $RbNbW_2O_9$ data are shown (see the supporting information for $KNbW_2O_9$ data). Key portions of the diffraction data are shown in Figs. 2(*a*) and 2(*b*). It can be readily seen that the peak observed at ~2.3 Å is modelled reasonably well by the introduction of the tilting modes. While both models give fits of a reasonable quality, the $\sqrt{3}a_0 \times 3a_0 \times 2c_0$ model appears to be the most promising due to an improved fit (χ^2) even though there are fewer variable atomic parameters (N_{tot}) as shown in Table 1. Switching of the *a* and *b* parameters relative to the published structure and a reduction in N_{tot} suggest that perhaps the starting model utilized by Chang *et al.* (2008) was incorrect and was more complex than required. The simplest reduction in complexity is a reduction in cell parameters to a unit cell with dimensions $\sqrt{3}a_0 \times a_0 \times 2c_0$ and subsequently $a_0 \times \sqrt{3}a_0 \times 2c_0$ for the model featuring switching of the *a* and *b* parameters. This corresponds to loss of an additional *irrep* at the K-point (**k** = $\frac{1}{3}$, $\frac{1}{3}$, 0) of the hexagonal parent Brillouin zone. The present diffraction data indeed contain no evidence for scattering at

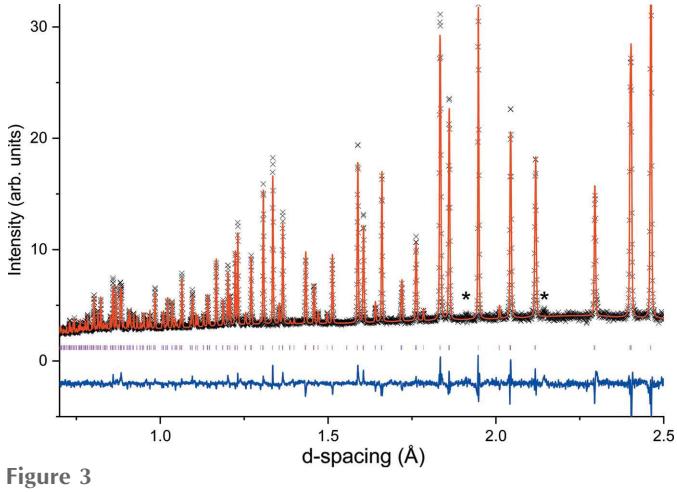

Figure 3
Portion of Rietveld refinement profile of $RbNbW_2O_9$ PND data at 288 K using the simplest $Cmc2_1$ model (cell metrics $a_0 \times \sqrt{3}a_0 \times 2c_0$). The peaks marked '*' indicate peaks that can be attributed to the vanadium can.

the K point. Despite both these simpler models having fewer refineable parameters than either of the larger cells, a significant improvement in the goodness-of-fit parameters Table 1 (and Table S1 for $KNbW_2O_9$) obtained from Rietveld refinement [Figs. 2(*c*) and 2(*d*)] is observed for both models. Of the two 'small cell' models, the second, featuring switching of the *a* and *b* parameters, results in a significantly better fit and is therefore more likely to be correct. The corresponding Rietveld fit to this model is shown in Fig. 3.

Further attempts to reduce the complexity of the system were carried out by considering the group–subgroup relationship between $Cmc2_1$ and the parent $P6/mmm$ (see Fig. S2). Although there are six possible space groups with a doubling of the *c* axis attributable to tilting, work by Chang *et al.* (2008) confirmed – using second-harmonic generation (SHG) measurements – that the structures adopted by both $RbNbW_2O_9$ and $KNbW_2O_9$ at ambient temperature result in a significant SHG signal, indicating a non-centrosymmetric phase. Hence, each of the non-polar phases can be discarded. As discussed previously, octahedral tilting can only be introduced *via* the A_3^+ and A_6^+ distortion modes, thus, only the orthorhombic space group $Cmc2_1$ and hexagonal space group $P6_3cm$ remain as possibilities. Comparison of the goodness-of-fit parameters obtained from Rietveld refinement (see Fig. S3 for refinement in $P6_3cm$) of both models indicates that $Cmc2_1$ results in a significantly better fit to the data for both compositions (χ^2 = 6.106 *versus* 39.76 in the case of $RbNbW_2O_9$). This indicates that the proposed orthorhombic $Cmc2_1$ model is adopted by both $RbNbW_2O_9$ and $KNbW_2O_9$ at ambient temperature. The crystal structure of the $Cmc2_1$ phase of $RbNbW_2O_9$ and $KNbW_2O_9$ is shown in Fig. 4 and the corresponding crystallographic data are presented in Tables 2 and S2. For comparative purposes, Rietveld refinement was carried out in the non-polar *Cmcm* model (Fig. S4) using the unit cell metrics of the best $Cmc2_1$ model. The goodness-of-fit parameters indicate that this model results in a poorer fit to the observed data than the polar $Cmc2_1$ (χ^2 = 9.572 *versus* 6.106). This was expected due to the lack of off-centering of the *B*-site cations (SOJT distortion) arising from the lack of any polar distortion modes and thus fixed atomic positions. The better fit to the polar $Cmc2_1$ model, complemented by the strong SHG signal observed by Chang *et al.* (2008), supports the assignment of the $Cmc2_1$ model at ambient temperature.

Using the *ISODISTORT* programme the magnitude of the distortion modes present in the $Cmc2_1$ phase of both $RbNbW_2O_9$ and $KNbW_2O_9$ were examined, compared with the centrosymmetric *Cmcm* model and the results summarized in Table 3. The Γ_1^+ mode (present in both the centrosymmetric and non-centrosymmetric models) corresponds to a symmetric breathing mode and therefore does not contribute to a polar structure. However, both the Γ_2^- and Γ_5^- modes are polar modes and are therefore not present in the *Cmcm* model. These modes are responsible for displacements along the *c* axis, particularly of the *B* cations from the barycentre of their octahedra. The difference between the two distortion modes is predominantly in the direction of this displacement. While Γ_2^- displaces atoms along the *c* axis in the same direction, Γ_5^- instead features antipolar displacements in *c*, resulting in an orthorhombic distortion of the unit cell. The magnitude and

Table 2
Crystallographic data for $RbNbW_2O_9$ at 288 K.

Refined in space group $Cmc2_1$ [*a* = 7.3391 (1), *b* = 12.6917 (2), *c* = 7.7886 (1) Å].

Atom	Wyckoff position	*x*	*y*	*z*	100 × U_{iso} (Å^2)
Rb1	4*a*	0	0.9959 (4)	0.2140 (11)	4.96 (10)
O1	4*a*	0	0.4781 (3)	0.2291 (11)	1.98 (12)
O2	8*b*	0.2737 (5)	0.2712 (2)	0.2370 (19)	1.97 (7)
O3	4*a*	0	0.2148 (9)	0.0194 (15)	1.88 (26)
O4	8*b*	0.6826 (9)	0.1042 (6)	0.0201 (10)	1.72 (17)
O5	4*a*	0	0.2111 (7)	0.4562 (15)	1.13 (19)
O6	8*b*	0.6861 (8)	0.1033 (5)	0.4646 (5)	0.82 (13)
Nb/W1	4*a*	0	0.5013 (5)	0.0248 (11)	1.47 (16)
Nb/W2	8*b*	0.2491 (3)	0.2501 (14)	0.9942 (17)	2.74 (12)

Table 3
Distortion mode amplitudes for the ambient-temperature structures of $RbNbW_2O_9$ and $KNbW_2O_9$ ($Cmc2_1$) and the centrosymmetric *Cmcm* model of $RbNbW_2O_9$.

'—' indicates the absence of this distortion mode.

	Amplitude (Å)		
Mode	$RbNbW_2O_9$ ($Cmc2_1$)	$KNbW_2O_9$ ($Cmc2_1$)	$RbNbW_2O_9$ (*Cmcm*)
Γ_1^+	0.013	0.027	0.029
Γ_2^-	0.464	0.579	–
Γ_5^-	0.286	0.262	–
A_3^+	0.211	0.269	0.157
A_6^+	0.750	0.938	0.746

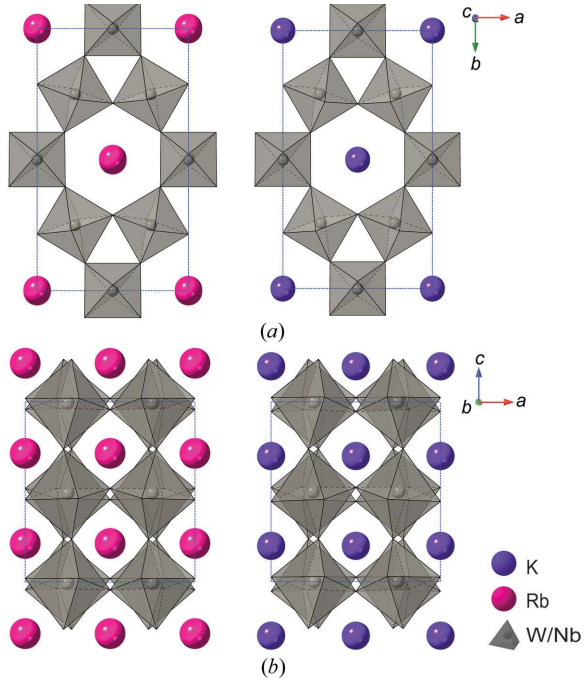

Figure 4
Crystal structures of the $Cmc2_1$ models adopted at 288 and 293 K by $RbNbW_2O_9$ (left) and $KNbW_2O_9$ (right), respectively, showing (*a*) the view down the polar *c* axis and (*b*) the view down the *b* axis; note the slightly different degree of octahedral tilting and *A* cation displacements.

direction of these displacements is shown in Fig. S5. Although both the A_3^+ and A_6^+ modes result in octahedral tilting, the mechanism is different for each. The A_3^+ mode corresponds to rigid tilting of the octahedra with alternating directions between layers, introducing a screw axis and subsequently the $(2c_0)$ unit cell expansion. However, the A_6^+ mode introduces tilting around different axes of the octahedra which results in the loss of the sixfold axis, distortion of the octahedra and subsequently an orthorhombic cell. While both A_3^+ and A_6^+ contribute to tilting of the $B1O_6$ octahedra, there is a much larger distortion of the $B2O_6$ octahedra due to the A_6^+ mode. The tilt pattern observed for both A modes from the parent *P*6/*mmm* structure has previously been reported by Campbell *et al.* (2018), albeit without the inclusion of the displacive Γ modes reported here.

3.2. Structural comparison of $RbNbW_2O_9$ and $KNbW_2O_9$

While the two compositions are isostructural, subtle differences are observed with regards to the magnitudes of the structural distortions; these are obviously driven by the different *A*-site cations, most likely by a purely size-related effect. This affects the structures in various ways: (i) the *A*-site cation is displaced in order to optimize its bonding environment; (ii) octahedral tilting occurs, cooperatively with this displacement, in order to optimize bonding around the *A* site (a similar effect to that which commonly occurs in the perovskite structure); (iii) the BO_6 octahedra distort slightly to accommodate the differing *A*-site cations (in addition to the inherent tendency for an off-centering of the *B*-site cations in both cases).

The changes in coordination environment around the *A* sites are shown in Fig. 5 and Table 4. In the ideal parent phase (*P*6/*mmm*) the 18-coordination of the *A* site can be regarded as '12 + 6', with the six longer bonds being those in the same *ab* plane as the *A* cation and the 12 shorter bonds being those from the symmetry-equivalent hexagonal rings above and below. In the observed ambient-temperature structures the environment becomes significantly distorted, with the same sets of *A*—O bond lengths showing a much wider spread. For $KNbW_2O_9$, for example, the coordination number might be regarded as 16 by defining a cut-off in the accepted K—O bond length for a bond valence of 0.01 valence units (∼3.85 Å). The improvement in bonding around the *A*-site cations, brought about by the observed structural distortions, can be seen by comparing the bond valence sums (BVSs) (Brese & O'Keeffe, 1991) for the ideal parent phase to the actual structures (Table 4). Even in the observed ambient-temperature structures there is still a considerable deviation from the ideal values (observed BVS values of 0.91 and 0.74 valence units for $RbNbW_2O_9$ and $KNbW_2O_9$, respectively). This severe underbonding of the *A*-site cations seems to be intrinsic to these HTB structures owing to the nature of the very large and quite rigid hexagonal channels.

Table 4
A-site bond lengths (Å) and bond valence sums (valence units) of $RbNbW_2O_9$ and $KNbW_2O_9$ calculated in an idealized non-polar *P*6/*mmm* model and in the orthorhombic $Cmc2_1$ phase at 288 and 293 K, respectively.

	$RbNbW_2O_9$		$KNbW_2O_9$	
Bond	'Ideal' *P*6/*mmm*	$Cmc2_1$ (288 K)	'Ideal' *P*6/*mmm*	$Cmc2_1$ (293 K)
A—O1	3.695 × 6	3.678 (1) × 2	3.689 × 6	3.688 (1) × 2
A—O2	3.330 × 12	3.305 (5) × 2	3.319 × 12	3.283 (7) × 2
A—O3		3.167 (11)		3.008 (11)
A—O3		3.579 (11)		3.727 (11)
A—O4		3.097 (7) × 2		2.959 (7) × 2
A—O4		3.567 (7) × 2		3.691 (8) × 2
A—O5		3.307 (11)		3.267 (11)
A—O5		3.319 (11)		3.336 (11)
A—O5		3.266 (6) × 2		3.244 (7) × 2
A—O6		3.313 (6) × 2		3.307 (7) × 2
BVS	0.80	0.91	0.57	0.74

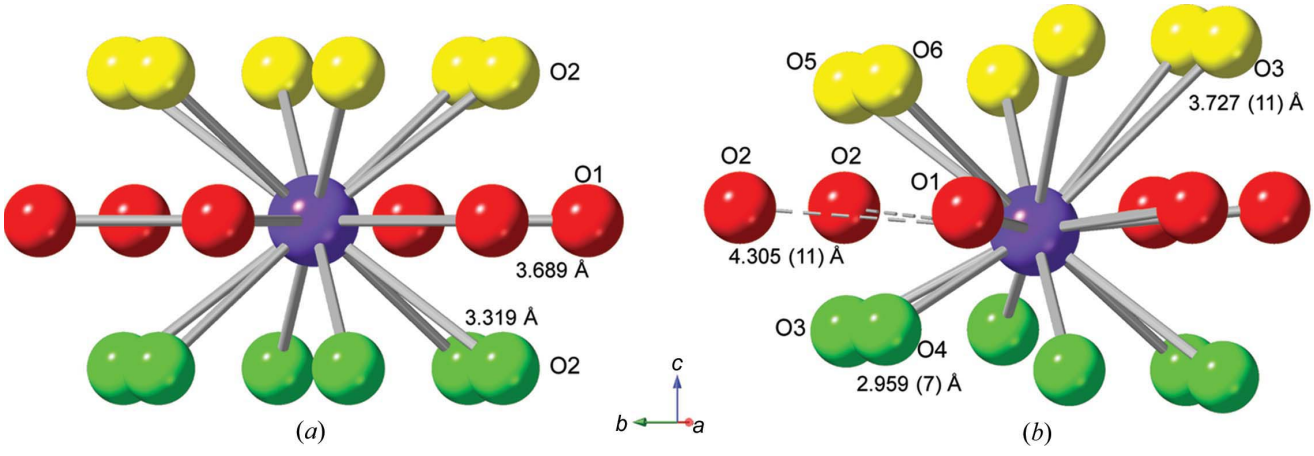

Figure 5
Schematic of the *A* site in $KNbW_2O_9$ in (*a*) the idealized *P*6/*mmm* and (*b*) $Cmc2_1$ phases, highlighting the displacement of the K^+ cation along the *c* axis and the subsequent change in the coordination environment from 18 to 16. The dashed bonds indicate the atoms that have a bond length above 3.85 Å and no longer contribute significantly to K—O bonding. The colours of the oxygen atoms correspond to the layers in the HTB structure; the green and yellow atoms correspond to the hexagonal rings above and below the *A*-site cation, respectively, and the red atoms are those in the same *ab* plane.

Table 5
Inter-octahedral bond angles of the $Cmc2_1$ phase of $RbNbW_2O_9$ and $KNbW_2O_9$ at 288 and 293 K, respectively.

$RbNbW_2O_9$		$KNbW_2O_9$	
B—O—B	Bond angle (°)	B—O—B	Bond angle (°)
$B1$—O1—$B1$	163.0 (2)	$B1$—O1—$B1$	158.5 (2)
$B1$—O6—$B1$	142.2 (7)	$B1$—O6—$B1$	139.7 (4)
$B2$—O2—$B2$	161.3 (1)	$B2$—O2—$B2$	156.83 (9)
$B2$—O3—$B2$	150.1 (11)	$B2$—O3—$B2$	148.3 (6)
$B2$—O4—$B2$	149.1 (8)	$B2$—O4—$B2$	147.3 (4)
$B2$—O5—$B2$	145.3 (11)	$B2$—O5—$B2$	142.6 (6)

Table 6
Octahedral distortion parameters for $RbNbW_2O_9$ and $KNbW_2O_9$ calculated from refinements of PND data collected at 288 and 293 K, respectively.

	$RbNbW_2O_9$		$KNbW_2O_9$	
Octahedra	Δ_1 (Å)	Δ_2 (°)	Δ_1 (Å)	Δ_2 (°)
$B1$	0.15	5.53	0.15	5.93
$B2$	0.027	0.93	0.054	2.33

As indicated previously, the magnitude of the peak at ~2.3 Å corresponding to octahedral tilting is greater in $KNbW_2O_9$ than $RbNbW_2O_9$. This greater degree of tilting, as shown in Fig. 4, unsurprisingly arises due to the smaller K^+ cation [$r(M^+)$ = 1.64 Å], providing less stabilization of the regularity of the hexagonal A-site channels compared with the larger Rb^+ cation [$r(M^+)$ = 1.72 Å]. Quoted ionic radii are for 12 coordination (Shannon, 1976). Selected bond angles associated with tilting are given in Table 5.

The degree of BO_6 octahedral distortion in each composition can be determined quantitatively based on deviations of the six bond lengths and the 12 bond angles (from 90°) from the mean values in each of the octahedra. This can be described in terms of the octahedral distortion parameter (Δ_1) and bond angle distortion (Δ_2), as defined by

$$\Delta_1 = \frac{1}{6}\Sigma\left|R_{av} - R_i\right|,$$
$$\Delta_2 = \frac{1}{12}\Sigma\left|90 - \varphi_i\right|,$$

where φ_i and R_i are the individual bond angles and bond lengths, R_{av} is the average bond length within the octahedron. The calculated octahedral distortions are presented in Table 6. It can be seen immediately that the $B1O_6$ octahedra in both $RbNbW_2O_9$ and $KNbW_2O_9$ are significantly distorted, but a greater bond angle distortion is observed in $KNbW_2O_9$. Perhaps more surprising is the considerable difference in values observed for the $B2O_6$ octahedra. While Δ_1 increases only slightly in $KNbW_2O_9$ relative to $RbNbW_2O_9$ (indicating that the $B2$ cations within the octahedra are more displaced within the K analogue); Δ_2 increases significantly in $KNbW_2O_9$. This is consistent with the significantly larger value observed for the amplitude of the Γ_2^- mode (Table 3), which describes the atomic displacements along the c axis, most notably of the B-site cation.

Table 7
B—O bond lengths of the $Cmc2_1$ phase of $RbNbW_2O_9$ and $KNbW_2O_9$ at 288 and 293 K, respectively.

$RbNbW_2O_9$		$KNbW_2O_9$	
B—O	Bond length (Å)	B—O	Bond length (Å)
$B1$—O1	1.618 (8)	$B1$—O1	1.605 (7)
$B1$—O1	2.318 (8)	$B1$—O1	2.337 (7)
$B1$—O3	1.872 (10) ×2	$B1$—O3	1.892 (6) ×2
$B1$—O4	1.961 (10) ×2	$B1$—O4	1.961 (6) ×2
$B2$—O3	1.89 (2)	$B2$—O3	1.871 (5)
$B2$—O2	2.028 (6)	$B2$—O2	2.087 (5)
$B2$—O4	1.93 (2)	$B2$—O4	1.934 (9)
$B2$—O5	1.93 (2)	$B2$—O5	1.957 (9)
$B2$—O6	1.93 (2)	$B2$—O6	1.897 (9)
$B2$—O2	1.919 (6)	$B2$—O2	1.888 (9)

A further consequence of the size difference between K^+ and Rb^+ (other than A-site displacements and octahedral tilting) is the difference in the axial (c axis) Nb/W—O bond lengths (given in Table 7), corresponding to the degree of SOJT distortion. As expected, the difference between axial bond lengths is greater in $KNbW_2O_9$ [0.732 ($B1$–O) and 0.216 Å ($B2$–O)] than in $RbNbW_2O_9$ [0.700 ($B1$–O) and ($B2$–O) 0.138 Å] indicating a greater degree of SOJT distortion in the K-analogue.

4. Conclusions

Using PND techniques, the ambient-temperature structures of the hexagonal tungsten bronzes $RbNbW_2O_9$ and $KNbW_2O_9$ have been shown to differ from the published $Cmm2$ structure ($3a_0 \times \sqrt{3}a_0 \times c_0$) derived from XRD (Chang *et al.*, 2008). Peaks corresponding to octahedral tilting, attributed to the A_6^+ and A_3^+ distortion modes, and subsequent c axis doubling were observed. The model suggested by Chang is also shown to be unnecessarily complex in a different respect, and the unit cell metrics in the ab plane are shown to be significantly smaller than previously proposed. In summary, both compositions have been shown to adopt a structure in the space group $Cmc2_1$ with unit cell metrics $a_0 \times \sqrt{3}a_0 \times 2c_0$ arising from a simple orthorhombic distortion of the aristotype $P6/mmm$ ($a_0 \times c_0$) structure. This distortion arises from a combination of octahedral tilting (A_6^+ and A_3^+) modes and a polar (displacive) mode (Γ_5^-). The distortions are driven by severe underbonding of the A-site cations coupled with the tendency for B-site 'off-centering' (SOJT) distortions. This study further emphasizes the need for neutron rather than X-ray diffraction coupled with the systematic application of symmetry-mode analysis to unambiguously solve structural problems of this type.

The research data supporting this publication can be accessed at https://doi.org/10.17630/17fd26d7-6099-4685-9762-f1a65b1e2d4e.

Funding information

We thank the Science and Technology Facilities Council (STFC) for the provision of neutron diffraction facilities at ISIS (HRPD experiment RB1710021, doi: 10.5286/

ISIS.E.RB1710021) and the School of Chemistry, University of St Andrews for funding of a studentship to JAM through the EPSRC doctoral training grant (grant No. EP/K503162/1).

References

Brese, N. E. & O'Keeffe, M. (1991). *Acta Cryst.* B**47**, 192–197.
Bursill, L. A., Julin, P., Braunshausen, G., Guangli, S. & Dryden, D. (1988). *Ferroelectrics*, **88**, 155–166.
Campbell, B., Howard, C. J., Averett, T. B., Whittle, T. A., Schmid, S., Machlus, S., Yost, C. & Stokes, H. T. (2018). *Acta Cryst.* A**74**, 408–424.
Campbell, B. J., Stokes, H. T., Tanner, D. E. & Hatch, D. M. (2006). *J. Appl. Cryst.* **39**, 607–614.
Chakhmouradian, A. R. & Woodward, P. M. (2014). *Phys. Chem. Miner.* **41**, 387–391.
Chang, H. Y., Sivakumar, T., Ok, K. M. & Halasyamani, P. S. (2008). *Inorg. Chem.* **47**, 8511–8517.
Ivanov, S. A., Sahu, J. R., Voronkova, V. I., Mathieu, R. & Nordblad, P. (2015). *Solid State Sci.* **40**, 44–49.
Kunz, M. & Brown, I. D. (1995). *J. Solid State Chem.* **115**, 395–406.
Larson, A. C. & Von Dreele, R. B. (2004). *General Structure Analysis System (GSAS)*. Report LAUR 86–748. Los Alamos National Laboratory, New Mexico, USA.
Li, L., Xu, H., Chen, Y. & Wang, Y. (2017). *Opt. Mater.* **66**, 361–366.
Lin, P. J. & Bursill, L. A. (1987). *Ferroelectrics*, **74**, 23–36.
Magnéli, A., Virtanen, A. I., Olsen, J., Virtanen, A. I. & Sörensen, N. A. (1953). *Acta Chem. Scand.* **7**, 315–324.
Maczka, M., Ko, J. H., Kojima, S., Majchrowski, A. & Hanuza, J. (2003). *J. Raman Spectrosc.* **34**, 371–374.
Shannon, R. D. (1976). *Acta Cryst.* A**32**, 751–767.
Simon, J. & Ravez, A. (2006). *C. R. Chim.* **9**, 1268–1276.
Toby, B. H. (2001). *J. Appl. Cryst.* **34**, 210–213.
Whittle, T. A., Schmid, S. & Howard, C. J. (2015). *Acta Cryst.* B**71**, 342–348.
Whittle, T. A., Schmid, S. & Howard, C. J. (2018). *Acta Cryst.* B**74**, 742–744.
Yanovsky, V. K., Voronkova, V. I. & Klimova, I. P. (1983). *Ferroelectrics*, **48**, 239–246.